HHS Public Access

Author manuscript

Biofouling. Author manuscript; available in PMC 2024 February 27.

Published in final edited form as:

Biofouling. 2023 January ; 39(1): 36–46. doi:10.1080/08927014.2023.2177538.

Effects of phosphate and silicate on stiffness and viscoelasticity of mature biofilms developed with simulated drinking water

Conghui Huang[1], **Gemma G. Clark**[1], **Farzana R. Zaki**[2], **Jungeun Won**[2,5], **Runsen Ning**[1], **Stephen A. Boppart**[2,4,5,6], **Ahmed E. Elbanna**[1], **Thanh H. Nguyen**[1,3,4]

[1]Department of Civil and Environmental Engineering, University of Illinois at Urbana Champaign, Urbana, IL

[2]Beckman Institute for Advanced Science and Technology, 405 North Mathews Avenue, Urbana, Illinois 61801, USA

[3]Institute of Genomic Biology, University of Illinois at Urbana-Champaign, Urbana, Illinois, 61801, United States

[4]Carle Illinois College of Medicine, University of Illinois at Urbana-Champaign, 506 South Mathews Avenue, Urbana, Illinois 61801, USA

[5]Department of Bioengineering, University of Illinois Urbana Champaign, 1304 West Springfield Avenue, Urbana, Illinois 61801, USA

[6]Department of Electrical and Computer Engineering, University of Illinois Urbana Champaign, 306 North Wright Street, Urbana, Illinois 61801, USA

Abstract

Biofilms, a porous matrix of cells aggregated with extracellular polymeric substances under the influence of chemical constituents in the feed water, can develop a viscoelastic response to mechanical stresses. In this study, the roles of phosphate and silicate, common additives in corrosion control and meat processing, on the stiffness, viscoelasticity, porous structure networks, and chemical properties of biofilm were investigated. Three-year biofilms on PVC coupons were grown from sand-filtered groundwater with or without one of the non-nutrient (silicate) or nutrient additives (phosphate or phosphate blends). Compared with non-nutrient additives, the phosphate and phosphate-blend additives led to a biofilm with the lowest stiffness, most viscoelastic, and more porous structure, including more connecting throats with greater equivalent radii. The phosphate-based additives also led to more organic species in the biofilm matrix than the silicate additive did. This work demonstrated that nutrient additives could promote biomass accumulation but also reduce mechanical stability.

Corresponding Author: Conghui Huang, chuang65@illinois.edu.

[5]Conflicts of interest

There are no conflicts of interest to declare.

1. Introduction

Biofilm, a porous matrix of aggregated microorganisms embedded in a network of extracellular polymeric substances (EPS) is ubiquitous in both natural and anthropogenic environments (Benoit et al. 2019; Penesyan et al. 2021). Biofilm properties, such as thickness, porosity, stiffness, and viscoelasticity, play an important role in biofilm growth, migration, and resilience in an aquatic environment (Peterson et al. 2015; Gloag et al. 2020; Nguyen et al. 2021). The water-filled porous networks in the biofilm matrix can contribute to the microorganism organization, which allows nutrient transport, cell signaling, and microbial competition (Coyte et al. 2017; Quan et al. 2022). These porous networks also influence the stiffness and mechanical stability of the biofilm matrix, which can lead to biofilm detachment and colonization on the downstream surfaces (Hozalski et al. 2020; Huang et al. 2020). Under the shear of water, more bacteria were released from simulated drinking water biofilms with lower stiffness (Shen et al. 2016; Shen et al. 2017). Biofilm grown on filter membrane surfaces can significantly influence the performance of these filters and increase the energy consumption and maintenance (Mansouri et al. 2010; Orgad et al. 2011; Ferrando Chavez et al. 2016; Vinagre et al. 2022). The ineffective penetration of antimicrobial or disinfectant chemicals into the biofilm matrix can prevent effective removal of biofilms and inhibit the inactivation of biofilm-associated pathogens (Corbin et al. 2011; He et al. 2013; Sun et al. 2021; Simões et al. 2022). In addition, energy dissipation by the biofilm viscoelastic behaviors can assist the biofilm matrix to adapt to mechanical stresses, allowing biofilm to propagate and persistently attach to the substratum (Gloag et al. 2020; Nguyen et al. 2021). Viscoelastic properties of the biofilm matrix can be attributed to the chemical composition of EPS, which is developed and adapted by the biofilm inhabitants under the influence of the growth conditions (Peterson et al. 2013). Thus, controlling biofouling and biofilm colonization in unfavorable conditions requires an understanding the biofilm structure and viscoelasticity.

Growing conditions, such as hydrodynamics, source water chemistry or nutrient conditions, disinfectants, growth period, and substratum material, have been identified as being key factors in biofilm physiology (Peterson et al. 2015; Shen et al. 2016; Gloag et al. 2020; Jara et al. 2021; Nguyen et al. 2021). For example, cation removal from groundwater continuously over 10 months led to multi-species biofilms with lower stiffness (Shen et al. 2018). In contrast, introducing cation, such as calcium, reduced the stiffness of single-species biofilms that were developed over only two days (Safari et al. 2014).Viscoelasticity and stiffness were associated with biofilm EPS production, composition, and overall porosity (Abe et al. 2011; Aggarwal and Hozalski 2012; Sweity et al. 2015; Ferrando Chavez et al. 2016; Horvat et al. 2019; Huang et al. 2020; Rahman et al. 2021). Under an elevated nutrient concentration, more viscoelastic behavior, lower stiffness, less EPS production, and fewer thickening processes were observed in single-species biofilms within three days of growth (Greener et al. 2016; Kundukad et al. 2016; Allen et al. 2018). However, the role of nutrient level on naturally grown biofilms porous structure and viscoelasticity has not been extensively studied. Controlling nutrients in the growing environment may be a viable strategy for preventing biofilm growth in unfavorable situations, such as drinking water distribution systems, healthcare equipment, and on

surfaces used in the food industry (Proctor CR et al. 2018; National Academies of Sciences et al. 2019; Proctor C et al. 2022). Phosphates, an important nutrient source for microorganisms, are commonly used as corrosion inhibitors in drinking water and food additives in meat processing (S. Mcneill and Edwards 2002; Thangavelu et al. 2019). Metasilicate, a non-nutrient additive, can serve as an alternative to phosphate as a corrosion inhibitior and an antimicrobial agent in meat processing (Sharma et al. 2012). Understanding the effects of nutrients on biofilm porous structure and viscoelasticity can help mitigate the risk of biofilm growth in drinking water and in the food industry.

The current research addresses the knowledge gaps mentioned above by determining the role of phosphate and metasilicate, a nutrient and non-nutrient additive, respectively, on biofilm structure and viscoelasticity. Specifically, the biofilm structure and pore network were characterized using image reconstructions with optical coherence tomography (OCT) and pore network analysis. Biofilm stiffness and viscoelasticity were determined using nanoindentation and analyzed with three classic contact mechanical models. The biofilm's porous structure and viscoelasticity can play an important role in the resistance of the mature and multi-species biofilms to mechanical removal. Therefore, this study aimed to determine the stiffness and viscoelasticity in biofilms developed with or without phosphate-based additives. These results may aid in the water quality management and developments in mechanical removal of biofilms in the drinking water and food industry.

2. Material and methods

2.1 Biofilm preparation

Four types of biofilms were grown on PVC coupons (12.7 mm in diameter, Biosurface Inc.) in four CDC reactors fed by groundwater with or without nutrient or non-nutrient additives. The influent groundwater, a local drinking water supply, was pumped from a well located in Urbana-Champaign, IL. This groundwater was filtered by a greensand filter, similar to the treatment method used at the local drinking water treatment facility, to remove precipitates from the oxidation of iron and manganese. Silicate, phosphate, and phosphate blends (6:4 molar ratio of disodium phosphate and sodium hexametaphosphate) were selected to simulate common corrosion inhibitor levels applied in many drinking water plants (S. Mcneill and Edwards 2002). Groundwater (10L) was mixed with disodium phosphate and sodium hexametaphosphate (2.4 mg L^{-1} as PO_4) or sodium metasilicate (20 mg L^{-1} as SiO_2) and served as influent to phosphate blends and silicate reactors, respectively. Disodium phosphate was mixed with 15L of groundwater to reach a final concentration of 2 mg L^{-1} as PO_4. The modified groundwater was prepared every two to three days. During biofilm formation, its structure and mechanical properties can change. For example, a soft top layer with increased thickness and biomass were reported in mature biofilms even though an increase in cell numbers was not observed (Martiny et al. 2003; Abe et al. 2011). The structural changes in three-year-old multispecies biofilms and succession events may not be predicted by biofilm formation models (Martiny et al. 2003; Sauer et al. 2022). The changes in mature biofilms can play an important role in the mechanical removal of biofilms in premise plumbing, which can be undisturbed for years. For example, a sanitary survey is required by the United States Environmental Protection Agency every

three years in community water systems (USEPA 2008). Hence the biofilms used in the study were allowed to develop for three years. Shear condition (Re = ~3510) in the CDC reactors was maintained by a stir bar during biofilm growth. The reactors were kept at around 25 °C and wrapped in foil.

2.2 Biofilm imaging by optical coherence tomography (OCT)

The biofilm structure of the four studied biofilms was characterized by cross-sectional scans with a dimension of 3.125 mm × 4.18 mm × 4 mm using a custom-built spectral-domain optical coherence tomography (SD-OCT) and the method described in a previous publication (Huang et al. 2020). A superluminescent diode with a center wavelength of 1325 nm and bandwidth = 100 nm (SLD1325 Thorlabs) was used with 1024-pixel InGaAs line-scan camera (SU-LDH2, Goodrich) for detection and a 2D galvanometer scanner (GVS102, Thorlabs) for scanning. The achromatic lens (f = 50 mm, Thorlabs) was used as the objective lens. The system was operated at a ~92 kHz line scan rate and had an axial resolution of ~8 μm and a lateral resolution of ~16 μm in air. Two to three locations were chosen randomly from each biofilm-covered coupon, and two to three coupons were imaged for each reactor. About 50–150 images from each imaged location were selected and processed based on the image quality. OCT images were corrected for orientation that was potentially introduced during image collection to reduce reflection caused by water using ImageJ (Fiji v 2.0) (Schindelin et al. 2012) and Avizo (Thermo Fisher Scientific). The biofilm thickness was determined using a MATLAB code described previously (Derlon et al. 2012; Shen et al. 2015). The PVC surface was identified and marked based on the location of the PVC edge in first image frame. The biofilm surface was determined by a thresholding algorithm using a modified version of the IsoData algorithm, which iteratively increased the threshold to above the composite average of the pixels in the background (at or below threshold) and in the biofilm surface (above threshold). The optical thickness of the biofilms was estimated by subtracting the height of the marked PVC surface from the height of the biofilm surface at each column along the horizontal axis of the OCT images. The optical thickness was divided by the corresponding refractive index from 1.33 to 1.38 to obtain the physical thickness. The average thickness of each biofilm image stack was then calculated as described previously (Huang et al. 2020). A layer of 690–720 μm from the maximum height of the biofilm surface in each OCT image stack was analyzed for overall porosities and pore structure as the OCT laser light could penetrate and produce high-quality images for these layers. Pores and throats with an equivalent radius lower than 5 μm, below the OCT image resolution of 8–10 μm, were removed from the analysis. Image analysis for pore structure was conducted using Avizo (Thermo Fisher Scientific) as described previously (Huang et al. 2020). Representative OCT images are shown in Figure 1S.

2.3 Biofilm chemical composition characterization using FTIR

The chemical composition of the biofilm developed under the influence of the nutrient or non-nutrient additives was characterized using a Fourier-transform infrared spectrophotometer equipped with an attenuated total reflection element (ATR-FTIR). Biomass was scraped from the biofilm-covered rods obtained from four CDC reactors and air-dried in clean Petri dishes overnight at 4 °C in dark. Two biomass samples from each reactor were subjected to FTIR scans. Twenty scans were taken for each biomass. Based

on these twenty scans, the infrared radiation (IR) absorbance profile over the wavenumber from 400 to 4000 cm^{-1} was collected. The potential chemical composition was characterized by comparing the wavenumber associated with the absorbance peaks with the IR spectrums reported in previous studies (Schmitt and Flemming 1998; Holman et al. 2009).

2.4 Biofilm mechanical property characterization using nanoindentation

Two to three coupons covered by each biofilm type were carefully removed from the reactors for nanoindentation measurement. Ten to twenty locations were randomly selected on a biofilm-covered coupon and subjected to nanoindentation measurement. A pre-calibrated cantilever with a stiffness of 0.49 N m^{-1} or 0.03N m^{-1} and a spherical glass probe with a radius of 25 or 9 μm were indented onto the biofilm surface. Before each experiment, the probe was calibrated on a clean petri dish bottom in a solution of groundwater amended with the corresponding nutrient or non-nutrient additives. The force and indentation depth over time were recorded during each indentation cycle. The approach and retraction velocity of the probe was set at 0.5, 1, 2, and 5 μm s^{-1} for each location. Two to four indentations were applied with each approach/retraction velocity at each location. Approximately 700 to 1100 force-indentation curves for each biofilm type were collected and analyzed. Contamination of the probe surface was identified by indenting the probe on a clean petri-dish surface in the solution conditions corresponding to biofilm growing conditions. Probe adhesion to this surface indicated potential contamination. A contaminated probe was discarded or cleaned with 70% ethanol until no adhering material was detected.

The mechanical properties of these biofilms were determined by fitting the indentation data to three types of models (Hertz's model, a viscoelastic model, and a hyperelastic model). First, Young's modulus was obtained from the Hertz model as equation 1.

$$F = \frac{4 \times E}{3 \times \left(1 - \nu^2\right)} \times \left(R \times d^3\right)^{1/2} \quad \text{Equation 1}$$

In this equation, F is the contact force; E is Young's modulus; d is the indentation; R is the probe radius, and ν is the Poisson's ratio and assumed to be 0.5 (soft material). However, after fitting the experimental data with the Hertz model, the Hertz model did not completely describe the force-indentation relationship during the indentation process for all locations (Table 1S). This incomplete description of the force-indentation relationship by the Hertz model may be caused by a large potential deformation induced by the probe during indentation. For this reason, the force-indentation curves were also fitted to a hyperelastic strain energy function (equation 2), developed by Fung (Fung 1967; Fung et al. 1979; Lin et al. 2008).

$$F = B\pi\left(\frac{a^5 - 15Ra^4 + 75R^2a^3}{5Ra^2 - 50R^2a + 125R^3}\right)\exp\left[b\left(\frac{a^3 - 15Ra^2}{25R^2a - 125R^3}\right)\right] \quad \text{Equation 2.1}$$

$$B = \frac{20E_0}{9\pi\left(1-\nu^2\right)} \quad \text{Equation 2.2}$$

$$a = (R\delta)^{1/2} \quad \text{Equation 2.3}$$

In these equations, E_0 is the instantaneous modulus, a is the Hertzian contact radius, and b is a fitting parameter from the analytical solution of the selected hyperelastic equation. The viscoelastic properties of the biofilms were also determined by fitting the time-dependent force-indentation curves to a one-element standard linear solids (SLS) model adapted in Ting's model,(Efremov et al. 2017) in which the time-dependent force-indentation curve is modeled with a spring arranged in parallel with a spring and dashpot system. A least-square fitting process using a trust-region-reflective algorithm was used to obtain the optimum set of the viscoelastic parameters when equation 3 was integrated numerically, following the methods reported in Efremove et al (Efremov et al. 2017). The Young's modulus obtained from the Hertz model served as an initial guess for both the instantaneous and long-term modulus in the fitting process with the viscoelastic model. Based on the fitting results obtained from preliminary experiments, 0.1 s was set as the initial guess for relaxation time, which is the time scale of stress relaxation in the SLS model. This value was in the range of the reported relaxation time from cultured biofilms (Andrews et al. 2013; Peterson et al. 2013). Poroelasticity models were not applied to the measured data because the relaxation times determined in the preliminary experiments were lower than the poroelasticity relaxation time of 10 to 100 s.(Hu and Suo 2012) The SLS model was selected over the power-law model for our biofilm measurements because the SLS model better described the force-indentation in the pre-analysis step.

$$F(t,\delta(t)) = \frac{4R^{1/2}}{3\left(1-\nu^2\right)}\int_0^t E(t-\xi)\frac{\partial\delta^{3/2}}{\partial\xi}d\xi \quad \text{Equation 3.1}$$

$$E(t) = E_\infty + (E_0 - E_\infty)\exp(-t/\tau) \quad \text{Equation 3.2}$$

In these equations, $F(t,\delta(t))$ is the time-dependent contact force and E(t) is the time-dependent modulus. Instantaneous modulus (E_0) and long-term modulus (E_{inf}) demonstrate the instant and long-term deformation upon being subject to pressure, respectively. The relaxation time (τ) demonstrates the viscoelastic properties of the biofilms. Indentation depths were below 10% of the average biofilm thickness, satisfying the shallow indentation assumption. A MATLAB (R2021a Update 4, Mathworks) code was written to analyze the force-indentation data.

2.5 Statistical analysis

The Kolmogorov-Smirnov test was used to compare the distributions of the average biofilm thickness, overall porosities, the pore and throats sizes, and parameters obtained from contact models and nanoindentations because of their non-normality. The student t-test was applied for data that passed the normality test and Levene's test for homogeneity of

variance. The difference was considered significant between distributions when a p-value was lower than 0.05. R (version 4.0.3) was used to conduct statistical analysis.

3. Results and Discussion

3.1 Phosphate nutrient additives led to organic species accumulation

The biofilm chemical composition was characterized by the IR absorbance profile obtained from the ATR-FTIR, and the results are shown in Figure 2S. Two distinctive absorbance profiles were observed between biofilms developed under the influence of phosphate or phosphate-free additives. Major absorbance peaks at around 710, 870, and 1400 cm^{-1} were found in the IR spectrums from groundwater biofilms and silicate biofilms, while no absorbance peak was associated with these wavenumbers in the IR spectrums from phosphate biofilms and phosphate blends biofilms. The absorbance peaks at the wavenumber of ~710 and 870 cm^{-1} were associated with aragonite and calcite, which were also found in groundwater biofilms in a previous study (Shen et al. 2018). The presence of aragonite and calcite can be attributed to the precipitation of divalent ions from groundwater. Also, absorbance peaks from 1020 to 1038 cm^{-1}, which were associated with phosphorus-containing compounds, were observed in the IR spectrums from phosphate biofilms and phosphate blends biofilms but not in the groundwater biofilms and silicate biofilms. Because FTIR absorbance cannot be used as a quantitative measure of concentrations, the absorbance ratios were used to compare the different species in the biofilms qualitatively. For example, the ratios of absorbance at 710 and 870 cm^{-1} compared to the absorbance peaks at 1020–1038 cm^{-1} can give relative comparison of aragonite and calcite over phosphorus-containing compounds. These ratios were 2.3 and 12.9 (groundwater biofilms) or 1.2 and 4.4 (silicate biofilms). The lack of the peaks at 710 and 871 cm^{-1} in IR spectrums from biofilms developed under the influence of phosphate can be attributed to the application of phosphate in drinking water as an anti-scaling additive, which reduces precipitation of divalent ions in hard drinking water. In addition, the IR spectrums showed different organic species could be found in biofilms developed with or without phosphate. Major absorbance bands were observed near 1640 cm^{-1} (amide I) and 1547 cm^{-1} (amide II) in biofilms under the influence of phosphate and blends of phosphate. These bands have previously been reported to be associated with proteins (Quilès et al. 2010; Pousti et al. 2018). However, no major absorbance bands were observed at these wavenumbers in groundwater and silicate biofilms. Minor absorbance peaks near 2920 and 2850 cm^{-1} associated with lipids (Pousti et al. 2018) were found in phosphate and blends of phosphate biofilms but not in biofilms without phosphate addition. These differences in absorbance peaks found in the biofilm with or without phosphate suggested that phosphate-based additives could promote organic species accumulation and reduce inorganic deposition. The accumulation of organic species and cross-link with biopolymer may contribute to biofilm thickness and stiffness of the top layer. These two biofilm properties were further explored.

3.2 Phosphate nutrient additives led to a porous biofilm with connecting pore structure

Overall, the biofilms developed with phosphate or phosphate blends were thicker and more porous than those developed in the groundwater with or without silicate additive (Figure 1a and b). Silicate biofilms were the thinnest among the four biofilms, followed by phosphate,

groundwater, and phosphate blends biofilms with a median of the average thickness of 481, 936, 1152, and 1204 μm, respectively. The median values of the overall porosities in the phosphate and phosphate blends biofilms were 0.29 (95% confidence interval (CI): 0.21–0.35) and 0.23 (95% CI: 0.13–0.38), respectively, and greater than those in silicate (0.12, 95% CI: 0.047–0.16) and groundwater (0.073, 95% CI: 0.022–0.13) biofilms ($p < 0.05$, KS test).

The biofilm pore structure was characterized by fitting a network of spherical pores and cylindrical throats to the pore spaces reconstructed from the OCT images. The sizes of the pores and throats were reported as pore equivalent radius and throat equivalent radius and length. Because these biofilms have different volumes, the values of the pore and the throat numbers were normalized by the corresponding biofilm volumes before conducting a statistical comparison. All four types of biofilms have similar values of normalized pore numbers (Figure 1c). However, more throats were found in the phosphate blends and phosphate biofilms than in the groundwater and silicate biofilms (KS test, $p < 0.05$). This suggested more connection among pores in the phosphate blend and phosphate biofilms. A larger median of pore equivalent radius was found in the groundwater biofilms (7.2 μm) than that in the biofilms grown with phosphate-based (phosphate: 6.5 μm and phosphate blends: 6.9 μm) or phosphate-free additives (6.2 μm) (KS test, $p < 0.05$) (Figure 3S). However, compared with groundwater biofilms (95% CI: 5.2–22 μm), the phosphate (95% CI: 5.2–45 μm) and phosphate blend (95% CI: 5.2–47 μm) biofilms have more pores with equivalent radii above the median. For example, phosphate blends and phosphate biofilms had approximately 2.8 and 2.5 times more pores with an equivalent radius greater than 30 μm than groundwater biofilms, respectively. As shown in Figure 4S, the throat equivalent radii were greater in phosphate biofilms (median: 19 μm, 95% CI: 6.4–47 μm), followed by that in phosphate blends biofilms (median: 18 μm, 95% CI: 6.3–46 μm), groundwater biofilms (median: 18 μm, 95% CI:6.1–40 μm), and silicate biofilms (median: 17 μm, 95% CI: 5.8–37 μm) ($p < 0.05$, KS test). However, the throat length in the silicate biofilms were the greatest (median: 167 μm, 95% CI: 60–404 μm), followed by phosphate blends biofilms (median:140 μm, 95% CI: 53–334 μm), then phosphate biofilms (median: 139 μm, 95% CI: 52–328 μm), and groundwater biofilms (median: 136 μm, 95% CI: 50–350 μm) ($p < 0.05$, KS test). A 3-D representation of the pore structure for these biofilms were also reconstructed. The representative pore network models (Figure 1 d to g) show that pores were isolated and scattered in silicate and groundwater biofilms. In comparison, phosphate and phosphate blends biofilms had more pores connected by throats with greater equivalent radii. Overall, more throats were found in phosphate and phosphate blends biofilm. These throats were longer than those in the groundwater biofilms but shorter than those in the silicate biofilms. However, the throats in the phosphate and phosphate blends biofilms were wider compared to those in the groundwater and silicate biofilms. Thick biofilms with a porous structure and wider connecting pore spaces can be attributed to greater organic species accumulation and less inorganic deposition under the influence of nutrient addition.

3.3 Phosphate nutrient additives promoted a softer and viscoelastic matrix

The mechanical properties, including instantaneous and long-term modulus and relaxation time for these four types of biofilms, were determined and are shown in Figure 2. The

goodness of fit to the Hertz model, hyperelastic model, and the viscoelastic model are shown in Figure 5S and Table 1S. First, the fitting of Young's modulus obtained by the Hertz model was discussed. In general, the distributions of the Young's modulus were wide and skewed to the right with smaller medians compared to means. As shown in Figure 2a, silicate biofilms were the stiffest, with a median Young's modulus of 3.7 kPa (5–95% CI: 0.37–19 kPa), followed by groundwater biofilms (median 1.8 kPa, 5–95% CI: 0.33–8.2 kPa). The phosphate and phosphate blend biofilms were significantly softer than those grown without phosphate-based additives ($p < 0.05$). The phosphate blends biofilms (median 0.51 kPa, 5–95% CI: 0.04–5.4 kPa) were significantly stiffer than the phosphate biofilms (median 0.39 kPa, 5–95% CI: 0.04–2.5 kPa) ($p < 0.05$). Thus, silicate biofilms can resist the most deformation under the same stress compared to those developed with phosphate-related additives.

Using the hyperelastic model, the silicate biofilms were the stiffest, with a median instantaneous elastic modulus of 4.1 kPa (95% CI: 0.2–28 kPa), followed by the groundwater biofilms with a median instantaneous elastic modulus of 2.4 kPa (95% CI: 0.4–12 kPa). The phosphate blends and phosphate biofilms have the lowest stiffness, with a median instantaneous modulus of 0.45 kPa (95% CI: 0.03–4.0 kPa) and 0.25 kPa (95% CI: 0.03–2.5 kPa), respectively. Also, the elastic modulus obtained from both the Hertz and the hypereslastic models can change over the range of approach and retraction velocity used in the experiment in part of the indented locations. However, there was no significant difference in the overall elastic moduli obtained from both models in all indented locations ($p > 0.05$), probably due to the heterogeneity of the biofilm surface structure.

A viscoelastic model (SLS model) that can describe the time-dependent force-indentation curves (Efremov et al. 2017) was used to investigate the influence of additives on biofilm viscoelastic properties. The trends of the instantaneous elastic modulus obtained from the viscoelastic model (SLS) agreed with the trends of elastic modulus for four biofilms obtained from the other two models (Figure 2a). The instantaneous modulus was the highest obtained from silicate biofilms, followed by the ones in groundwater biofilms and then those in phosphate blends and phosphate biofilms. Thus, silicate additive application in drinking water can result in a stiffer biofilm than biofilms developed with or without phosphate-based nutrient additives. The silicate biofilms may better resist the physical stress which causes deformation and detachment in premise plumbing systems. This observation was consistent with previous findings that showed cultivated biofilms in nutrient-rich media demonstrated more viscoelastic growth than those cultivated in nutrient-poor media (Rühs et al. 2013) and the structural arrangement of organic components in the EPS matrix (Shen et al. 2018).

Next, the effects of nutrient additives on biofilm relaxation time, a viscoelastic parameter demonstrating the recovery of biofilm structure under applied stress were determined. The relaxation times were statistically longest in phosphate biofilms with a median of 0.46 s (95% CI: 1×10^{-10}-10 s), followed by those in phosphate blends biofilms with a median of 0.11 s (95% CI: $\times 10^{-12}$-12 s) ($p < 0.05$). The relaxation times in silicate biofilms and groundwater biofilms were not significantly different ($p > 0.05$), but they were both significantly lower compared to the biofilms grown under the influence of phosphate with a median of 9×10^{-6} s (95% CI: 2×10^{-14}-4.4 s) and 8×10^{-6} (95% CI: 2×10^{-14}-4.0 s),

respectively. Previous studies have shown that a higher divalent ion concentration in the water can lead to stiffer and less viscoelastic biofilms compared to a lower divalent ion concentration in the feed water (Cao et al. 2016; Shen et al. 2018; Rahman et al. 2021). The less viscoelastic biofilm developed in groundwater without phosphate-containing additives may be due to greater water flow restriction in the less porous structure compared to those developed in groundwater with phosphate-containing additives.

As shown in Figure 2b, the relaxation time was distributed into two clusters, ranging from 10^{-14} to 10^{-2} (lower) and 10^{-2} to 12 s (upper) for all four biofilms. The relaxation time in the lower cluster (10^{-14} to 10^{-2} s) demonstrated the near-instantaneous recovery from indentations. Approximately 57% and 75% of the relaxation time obtained from the phosphate blends and phosphate biofilms were greater than 10^{-2} s, with a median of 1.0 s (95% CI: 0.05–27 s) and 0.91s (95% CI: 0.05–14 s), respectively. However, 37% and 35% of relaxation time determined in silicate and groundwater biofilms were greater than 0.01 s, with a median of 0.8 s (95% CI: 0.03–9.3 s) and 0.99 s (95% CI: 0.05–9.1s), respectively. Only 1.4%, 1.8%, 6%, and 5% of the measurements for groundwater, silicate, phosphate, and phosphate blend were higher than 10 s, which may be considered poroelasticity. These two clusters observed in all four biofilms can be attributed to the heterogeneity of the surface structure and the presence and composition of the EPS matrix in the biofilms (Peterson et al. 2013; Peterson et al. 2015). These relaxation times were within the range of relaxation times previously reported from mono-species biofilms (Peterson et al. 2013; Peterson et al. 2015). The current results show that the phosphate and phosphate blend biofilms demonstrated a longer overall relaxation time than biofilms developed in the absence of nutrient additives. Thus, compared to the other biofilms, the phosphate and phosphate blends biofilms demonstrated more viscoelastic behavior, which can contribute to the detachment and transport of the biomass. In addition, the biomass accumulation and connecting pore space developed under the phosphate additives can lead to biofilms with a reduced stiffness and increased viscoelasticity.

4. Conclusions

In this study, the chemical composition, stiffness and viscoelasticity of four multi-species biofilms developed with or without phosphate, as one of the important nutrient sources for microorganisms, were characterized after three years of growth. Phosphate and phosphate blends led to a porous biofilm structure with more large and wide connecting throats compared to biofilms developed without nutrient additives. In addition, adding phosphate-based additives reduced the stiffness and increased the viscoelasticity of biofilms. These characteristics may contribute to the efficacy of the mechanical removal of biofilms. In conclusion, the results demonstrate the role of phosphate on the structure and viscoelasticity of mature multi-species biofilms and the implications for the mechanical removal of these biofilms.

Supplementary Material

Refer to Web version on PubMed Central for supplementary material.

Acknowledgements

We acknowledge partial support from NSF grant 1855609. We thank Dr. Rosa M. Espinosa Marzal and Dr. Mengwei Han (UIUC) for the FTIR scans, Dr. Nicolas Derlon and Professor Eberhard Morgenroth (Eawag) for the MATLAB code used for OCT image analysis.

7. Reference:

Abe Y, Polyakov P, Skali-Lami S, Francius G. 2011. Elasticity and physico-chemical properties during drinking water biofilm formation. Biofouling 27(7):739–750. [PubMed: 21762041]

Aggarwal S, Hozalski RM. 2012. Effect of strain rate on the mechanical properties of *Staphylococcus epidermidis* biofilms. Langmuir 28(5):2812–2816. [PubMed: 22217007]

Allen A, Habimana O, Casey E. 2018. The effects of extrinsic factors on the structural and mechanical properties of *Pseudomonas* fluorescens biofilms: A combined study of nutrient concentrations and shear conditions. Colloids and Surfaces B: Biointerfaces 165:127–134. [PubMed: 29471219]

Andrews JW, Bowen J, Cheneler D. 2013. Optimised determination of viscoelastic properties using compliant measurement systems [10.1039/C3SM50706H]. Soft Matter 9(23):5581–5593.

Benoit DSW, Sims KR, Fraser D. 2019. Nanoparticles for Oral Biofilm Treatments. ACS Nano 13(5):4869–4875. [PubMed: 31033283]

Cao H, Habimana O, Safari A, Heffernan R, Dai Y, Casey E. 2016. Revealing region-specific biofilm viscoelastic properties by means of a micro-rheological approach. npj Biofilms and Microbiomes 2(1):5. [PubMed: 28649399]

Corbin A, Pitts B, Parker A, Stewart PS. 2011. Antimicrobial penetration and efficacy in an in vitro oral biofilm model. Antimicrobial Agents and Chemotherapy 55(7):3338–3344. [PubMed: 21537022]

Coyte KZ, Tabuteau H, Gaffney EA, Foster KR, Durham WM. 2017. Microbial competition in porous environments can select against rapid biofilm growth. Proceedings of the National Academy of Sciences 114(2):E161–E170.

Declerck P 2010. Biofilms: The environmental playground of *Legionella pneumophila*. Environmental Microbiology 12(3):557–566. [PubMed: 19678829]

Declerck P, Behets J, Margineanu A, van Hoef V, De Keersmaecker B, Ollevier F. 2009. Replication of *Legionella pneumophila* in biofilms of water distribution pipes [Article]. Microbiological Research 164(6):593–603. English. [PubMed: 17644359]

Derlon N, Peter-Varbanets M, Scheidegger A, Pronk W, Morgenroth E. 2012. Predation influences the structure of biofilm developed on ultrafiltration membranes. Water Res 46(10):3323–3333. eng. [PubMed: 22534121]

Efremov YM, Wang W-H, Hardy SD, Geahlen RL, Raman A. 2017. Measuring nanoscale viscoelastic parameters of cells directly from AFM force-displacement curves. Scientific Reports 7(1):1541. [PubMed: 28484282]

Ferrando Chavez DL, Nejidat A, Herzberg M. 2016. Viscoelastic properties of extracellular polymeric substances can strongly affect their washing efficiency from reverse osmosis Membranes. Environmental Science & Technology 50(17):9206–9213. [PubMed: 27404109]

Fung YC. 1967. Elasticity of soft tissues in simple elongation. Am J Physiol 213(6):1532–1544. eng. [PubMed: 6075755]

Fung YC, Fronek K, Patitucci P. 1979. Pseudoelasticity of arteries and the choice of its mathematical expression. Am J Physiol 237(5):H620–631. eng. [PubMed: 495769]

Gloag ES, Fabbri S, Wozniak DJ, Stoodley P. 2020. Biofilm mechanics: Implications in infection and survival. Biofilm 2:100017. [PubMed: 33447803]

Greener J, Gashti MP, Eslami A, Zarabadi MP, Taghavi SM. 2016. A microfluidic method and custom model for continuous, non-intrusive biofilm viscosity measurements under different nutrient conditions. Biomicrofluidics 10(6):064107. [PubMed: 27965730]

He Y, Peterson BW, Jongsma MA, Ren Y, Sharma PK, Busscher HJ, van der Mei HC. 2013. Stress relaxation analysis facilitates a quantitative approach towards antimicrobial penetration into biofilms. PLOS ONE 8(5):e63750. [PubMed: 23723995]

Holman H-YN, Miles R, Hao Z, Wozei E, Anderson LM, Yang H. 2009. Real-time chemical imaging of bacterial activity in biofilms using open-channel microfluidics and synchrotron FTIR spectromicroscopy. Analytical Chemistry 81(20):8564–8570. [PubMed: 19775125]

Horvat M, Pannuri A, Romeo T, Dogsa I, Stopar D. 2019. Viscoelastic response of Escherichia coli biofilms to genetically altered expression of extracellular matrix components [10.1039/C9SM00297A]. Soft Matter 15(25):5042–5051. [PubMed: 31179461]

Hozalski RM, LaPara TM, Zhao X, Kim T, Waak MB, Burch T, McCarty M. 2020. Flushing of stagnant premise water systems after the COVID-19 shutdown can reduce infection risk by *Legionella* and *Mycobacterium spp*. Environmental Science & Technology 54(24):15914–15924. [PubMed: 33232602]

Hu Y, Suo Z. 2012. Viscoelasticity and poroelasticity in elastomeric gels. Acta Mechanica Solida Sinica 25(5):441–458.

Huang C, Sun PP, Won J, Wang Y, Boppart SA, Nguyen TH. 2020. Effect of nonphosphorus corrosion inhibitors on biofilm pore structure and mechanical properties. Environmental Science & Technology 54(22):14716–14724. [PubMed: 33124800]

Jara J, Alarcón F, Monnappa AK, Santos JI, Bianco V, Nie P, Ciamarra MP, Canales Á, Dinis L, López-Montero I et al. 2021. Self-Adaptation of Pseudomonas fluorescens Biofilms to Hydrodynamic Stress [Original Research]. Front Microbiol 11. English.

Kundukad B, Seviour T, Liang Y, Rice SA, Kjelleberg S, Doyle PS. 2016. Mechanical properties of the superficial biofilm layer determine the architecture of biofilms [10.1039/C6SM00687F]. Soft Matter 12(26):5718–5726. [PubMed: 27273453]

Lin DC, Shreiber DI, Dimitriadis EK, Horkay F. 2008. Spherical indentation of soft matter beyond the Hertzian regime: numerical and experimental validation of hyperelastic models. Biomechanics and Modeling in Mechanobiology 8(5):345. [PubMed: 18979205]

Mansouri J, Harrisson S, Chen V. 2010. Strategies for controlling biofouling in membrane filtration systems: challenges and opportunities [10.1039/B926440J]. Journal of Materials Chemistry 20(22):4567–4586.

Martiny AC, Jørgensen TM, Albrechtsen H-J, Arvin E, Molin S. 2003. Long-term succession of structure and diversity of a biofilm formed in a model drinking water distribution system. Applied and Environmental Microbiology 69(11):6899–6907. [PubMed: 14602654]

National Academies of Sciences E, Medicine, Health, Medicine D, Division on E, Life S, Board on Population H, Public Health P, Board on Life S, Water S et al. 2019. Management of Legionella in Water Systems Washington (DC): National Academies Press (US) Copyright 2020 by the National Academy of Sciences. All rights reserved.

Nguyen H, Ybarra A, Başağaoğlu H, Shindell O. 2021. Biofilm viscoelasticity and nutrient source location control biofilm growth rate, migration rate, and morphology in shear flow. Sci Rep 11(1):16118. [PubMed: 34373534]

Orgad O, Oren Y, Walker SL, Herzberg M. 2011. The role of alginate in *Pseudomonas aeruginosa* EPS adherence, viscoelastic properties and cell attachment. Biofouling 27(7):787–798. [PubMed: 21797737]

Penesyan A, Paulsen IT, Kjelleberg S, Gillings MR. 2021. Three faces of biofilms: a microbial lifestyle, a nascent multicellular organism, and an incubator for diversity. npj Biofilms and Microbiomes 7(1):80. [PubMed: 34759294]

Peterson BW, He Y, Ren Y, Zerdoum A, Libera MR, Sharma PK, van Winkelhoff A-J, Neut D, Stoodley P, van der Mei HC et al. 2015. Viscoelasticity of biofilms and their recalcitrance to mechanical and chemical challenges. FEMS Microbiol Rev 39(2):234–245. [PubMed: 25725015]

Peterson BW, Mei HCvd, Sjollema J, Busscher HJ, Sharma PK, Chapman M, Hultgren SJ. 2013. A distinguishable role of eDNA in the viscoelastic relaxation of biofilms. mBio 4(5):e00497–00413. [PubMed: 24129256]

Pousti M, Joly M, Roberge P, Amirdehi MA, Bégin-Drolet A, Greener J. 2018. Linear Scanning ATR-FTIR for Chemical Mapping and High-Throughput Studies of *Pseudomonas sp.* Biofilms in Microfluidic Channels. Analytical Chemistry 90(24):14475–14483. [PubMed: 30449089]

Proctor C, Garner E, Hamilton KA, Ashbolt NJ, Caverly LJ, Falkinham JO, Haas CN, Prevost M, Prevots DR, Pruden A et al. 2022. Tenets of a holistic approach to drinking water-associated

pathogen research, management, and communication. Water Research 211:117997. [PubMed: 34999316]

Proctor CR, Reimann M, Vriens B, Hammes F. 2018. Biofilms in shower hoses. Water Research 131:274–286. [PubMed: 29304381]

Quan K, Hou J, Zhang Z, Ren Y, Peterson BW, Flemming H-C, Mayer C, Busscher HJ, van der Mei HC. 2022. Water in bacterial biofilms: pores and channels, storage and transport functions. Critical Reviews in Microbiology 48(3):283–302. [PubMed: 34411498]

Quilès F, Humbert F, Delille A. 2010. Analysis of changes in attenuated total reflection FTIR fingerprints of *Pseudomonas fluorescens* from planktonic state to nascent biofilm state. Spectrochimica Acta Part A: Molecular and Biomolecular Spectroscopy 75(2):610–616. [PubMed: 20004611]

Rahman MU, Fleming DF, Sinha I, Rumbaugh KP, Gordon VD, Christopher GF. 2021. Effect of collagen and EPS components on the viscoelasticity of Pseudomonas aeruginosa biofilms [10.1039/D1SM00463H]. Soft Matter 17(25):6225–6237. [PubMed: 34109345]

Rühs PA, Böni L, Fuller GG, Inglis RF, Fischer P. 2013. In-Situ quantification of the interfacial rheological response of bacterial biofilms to environmental stimuli. PLOS ONE 8(11):e78524. [PubMed: 24244319]

Mcneill LS, Edwards M 2002. Phosphate inhibitor use at US utilities Vol. 94.

Safari A, Habimana O, Allen A, Casey E. 2014. The significance of calcium ions on *Pseudomonas fluorescens* biofilms – a structural and mechanical study. Biofouling 30(7):859–869. [PubMed: 25115520]

Sauer K, Stoodley P, Goeres DM, Hall-Stoodley L, Burmølle M, Stewart PS, Bjarnsholt T. 2022. The biofilm life cycle: expanding the conceptual model of biofilm formationt Nature Reviews Microbiology 20(10):608–620. [PubMed: 35922483]

Schindelin J, Arganda-Carreras I, Frise E, Kaynig V, Longair M, Pietzsch T, Preibisch S, Rueden C, Saalfeld S, Schmid B et al. 2012. Fiji: an open-source platform for biological-image analysis. Nature Methods 9(7):676–682. [PubMed: 22743772]

Schmitt J, Flemming H-C. 1998. FTIR-spectroscopy in microbial and material analysis. International Biodeterioration & Biodegradation 41(1):1–11.

Sharma CS, Williams SK, Schneider KR, Schmidt RH, Rodrick GE. 2012. Antimicrobial Effects of Sodium Metasilicate Against *Listeria monocytogenes*. Foodborne Pathogens and Disease 9(9):822–828. [PubMed: 22889042]

Shen Y, Huang C, Lin J, Wu W, Ashbolt NJ, Liu W-T, Nguyen TH. 2017. Effect of disinfectant exposure on *Legionella pneumophila* associated with simulated drinking water biofilms: release, inactivation, and infectivity. Environmental Science & Technology

Shen Y, Huang C, Monroy GL, Janjaroen D, Derlon N, Lin J, Espinosa-Marzal R, Morgenroth E, Boppart SA, Ashbolt NJ et al. 2016. Response of simulated drinking water biofilm mechanical and structural properties to long-term disinfectant exposure. Environ Sci Technol 50(4):1779–1787. [PubMed: 26756120]

Shen Y, Huang PC, Huang C, Sun P, Monroy GL, Wu W, Lin J, Espinosa-Marzal RM, Boppart SA, Liu W-T et al. 2018. Effect of divalent ions and a polyphosphate on composition, structure, and stiffness of simulated drinking water biofilms. npj Biofilms Microbiomes 4(1):15. [PubMed: 30038792]

Shen Y, Monroy GL, Derlon N, Janjaroen D, Huang C, Morgenroth E, Boppart SA, Ashbolt NJ, Liu W-T, Nguyen TH. 2015. Role of biofilm roughness and hydrodynamic conditions in *Legionella pneumophila* adhesion to and detachment from simulated drinking water biofilms. Environmental science & technology 49(7):4274–4282. [PubMed: 25699403]

Simões LC, Gomes IB, Sousa H, Borges A, Simões M. 2022. Biofilm formation under high shear stress increases resilience to chemical and mechanical challenges. Biofouling 38(1):1–12. [PubMed: 34818957]

Sun PP, Won J, Choo-Kang G, Li S, Chen W, Monroy GL, Chaney EJ, Boppart SA, Eden JG, Nguyen TH. 2021. Inactivation and sensitization of Pseudomonas aeruginosa by microplasma jet array for treating otitis media. npj Biofilms and Microbiomes 7(1):48. [PubMed: 34078901]

Sweity A, Zere TR, David I, Bason S, Oren Y, Ronen Z, Herzberg M. 2015. Side effects of antiscalants on biofouling of reverse osmosis membranes in brackish water desalination. Journal of Membrane Science 481:172–187.

Thangavelu KP, Kerry JP, Tiwari BK, McDonnell CK. 2019. Novel processing technologies and ingredient strategies for the reduction of phosphate additives in processed meat. Trends in Food Science & Technology 94:43–53.

mUSEPA. 2008. Sanitary survey guidance manual for ground water systems. In: USEPA, editor

Vinagre PA, Lindén JB, Mardaras E, Pinori E, Svenson J. 2022. Probing the correlation between corrosion resistance and biofouling of thermally sprayed metallic substrata in the field. Biofouling 38(2):147–161. [PubMed: 35184621]

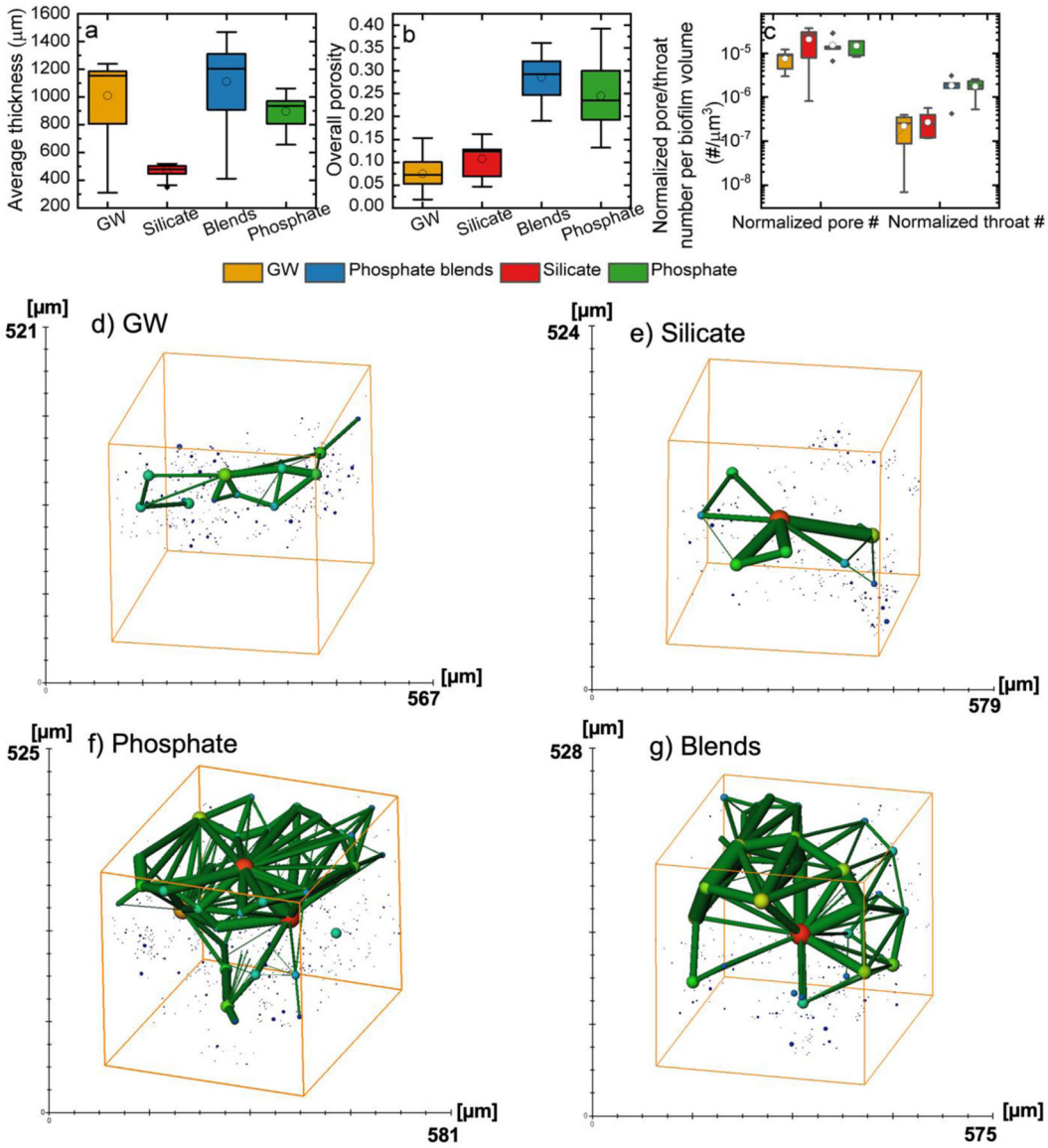

Figure 1.

Biofilm mean absolute thickness (**a**) (N = 195–673) and mean overall porosities (**b**) (N = 13–24) in the 720 μm surface layer of groundwater (yellow), silicate (red), phosphate blends (blue), and phosphate (green) biofilms. **c)** Distributions of normalized pore or throat number per biofilm volume (N = 5–7) in groundwater (yellow), silicate (red), phosphate blends (blue), and phosphate (green) biofilms. The pore network (spherical pores connected with cylindrical throats) obtained from the reconstructed pore space from **(d)** groundwater, **(e)** silicate, **(f)** phosphate, and **(g)** phosphate blends biofilms. The solid lines in the boxes marked the medians in the distributions. The boxes marked 25 to 75% of the percentile in the measurements. The whiskers are 1.5 interquartile range (IQR). Solid points are outliers and opened circles are means.

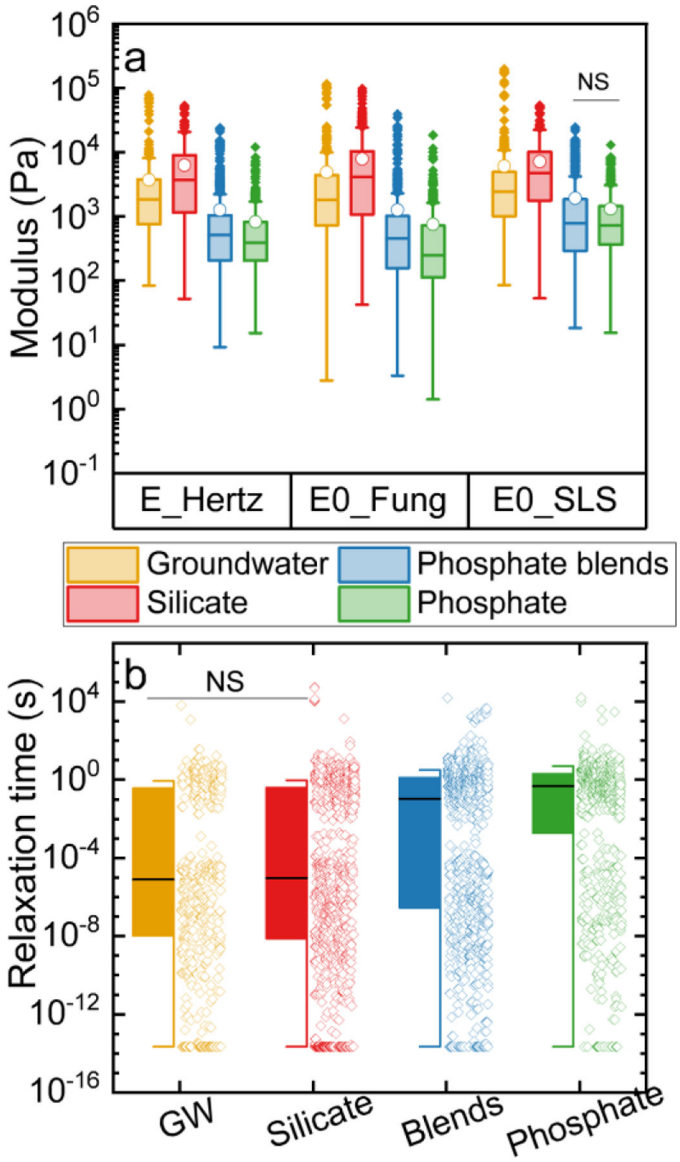

Figure 2.

a) Distributions of Young's modulus obtained by the Hertz model and instantaneous modulus obtained by the Fung model and SLS model (N = 633–1117). The solid lines in the boxes marked the medians in the distributions. The boxes marked 25 to 75% of the percentile in the measurements. The whiskers are 1.5 interquartile range (IQR). Solid points are outliers. NS indicates that no significant differences ($p > 0.05$) were found in the hypothesis test. **b)** Distributions of relaxation times obtained from the SLS model are shown for groundwater (yellow), silicate (red), phosphate blends (blue), and phosphate (green) biofilms (N = 633–1117). Solid black lines are medians of the relaxation times. Open circles are the relaxation time data points. Solid boxes mark the 25 to 75% percentiles of the relaxation time. The whiskers are 1.5 interquartile range (IQR). NS indicates that no significant differences ($p > 0.05$) were found in the hypothesis test.